Available online at www.sciencedirect.com
SCIENCE DIRECT®
Journal of Nuclear Materials 327 (2004) 58–76
journal of nuclear materials
www.elsevier.com/locate/jnucmat

# Effect of burn-up on the thermal conductivity of uranium dioxide up to 100.000 MWd t$^{-1}$

C. Ronchi [a,*], M. Sheindlin [a], D. Staicu [a], M. Kinoshita [b]

[a] European Commission, Joint Research Centre, Institute for Transuranium Elements, P.O. Box 2340, 76125 Karlsruhe, Germany
[b] Komae Research Laboratory, Nuclear Energy Systems Department, Central Research Institute of Electric Power Industry, 2-11-1 Iwado Kita, Komae-shi, Tokyo 201, Japan

Received 22 July 2003; accepted 31 January 2004

**Abstract**

The thermal diffusivity and specific heat of reactor-irradiated $UO_2$ fuel have been measured. Starting from end-of-life conditions at various burn-ups, measurements under thermal annealing cycles were performed in order to investigate the recovery of the thermal conductivity as a function of temperature. The separate effects of soluble fission products, of fission gas frozen in dynamical solution and of radiation damage were determined. In this context, particular emphasis was given to the behaviour of samples displaying the high burn-up rim structure. Recovery stages could be thoroughly investigated in samples that were irradiated at low burn-ups and/or at high irradiation temperatures. Other samples, in particular those exhibiting the characteristic rim structure, disintegrated at temperatures slightly higher than the irradiation temperature. Finally, from a database of several thousand measurements, an accurate formula for the in-pile thermal conductivity of $UO_2$ up to 100 GWd t$^{-1}$ was developed, taking into account all the relevant effects and structural changes induced by reactor burn-up.


## 1. Introduction

In the 5th Framework Research Programme of the European Commission (1997–2002) under the priority 'Safety of the Nuclear Fuel Cycle' a project was started at the Joint Research Centre, Institute for Transuranium Elements (JRC-ITU), whose aim was to perform a systematic measurement campaign on the thermal transport performance of irradiated light water reactor (LWR) fuel. The study was focused first on the behaviour of the thermal conductivity of $UO_2$ in the useful range of irradiation temperatures, including mild temperature transient conditions. Thermal diffusivity and specific heat measurements were therefore performed, in conjunction with post-irradiation examinations: optical ceramography, electron microscopy, mass spectrometry (MS), X-ray diffraction (XRD); and characterisation of fission product (FP) behaviour (density, swelling, concentration profiles of FP measured by energy dispersive X-ray analysis and electron-probe micro-analysis (EPMA), Knudsen-cell release and effusion processes). At present, the experimental database obtained consists of several thousand measurements, from which the deterioration of the fuel thermal conductivity with burn-up can be thoroughly analysed as a function of the fuel irradiation parameters.

## 2. Experiment

### 2.1. Samples

The objective of this work was to investigate the deterioration of the thermal conductivity of the $UO_2$

* Corresponding author. Tel.: +49-7247 951 402; fax: +49-7247 951 99402.
*E-mail address:* ronchi@itu.fzk.de (C. Ronchi).

0022-3115/$ - see front matter © 2004 Elsevier B.V. All rights reserved.
doi:10.1016/j.jnucmat.2004.01.018

fuel as a function of the irradiation conditions up to burn-ups of the order of 100 GWd t$^{-1}$. In this perspective, the first problem concerned the choice of representative samples in view of defining a parameterisation criterion for the irradiation conditions. Though fuel from commercial LWRs was preferred, as it is representative for the current irradiation conditions, parameterisation of the in-pile temperature history of a specimen taken from a fuel rod is not straightforward, and, in addition, can only be made based on model predictions. Therefore, only part of the samples were taken from standard fuel rods irradiated from 30 to 100 GWd t$^{-1}$, distinguishing between those taken from the pellet outer ring (irradiation temperature $T_{irr} \approx 600$–800 K) and those taken from the centre of the pellet ($T_{irr} \approx 1300$–1500 K). Other samples were provided by the CRIEPI High Burn-up Rim Project (HBRP). These were in the form of 1 mm thick disks, irradiated in the Halden reactor under constant, controlled temperature ($T_{irr}$ from 770 to 1470 K) and up to different burn-ups ranging from 34 to 96 GWd t$^{-1}$. In this capsule irradiation, each disk was pressed between two metallic plates, so that the temperature profile in the disk was sufficiently flat to justify the assumption of effectively isothermal irradiation conditions. Fuel enrichment and neutron spectra were chosen to achieve pre-fixed target burn-ups which were verified by post-irradiation EPMA and MS examinations. The irradiation time was the same for all the samples; different burn-ups were obtained at different positions in the reactor [1]. A description of the HBRP samples is given in Table 1. Altogether, 50 samples were selected, covering an ample range of irradiation parameters.

### 2.2. Experimental set-up and measurement procedure

A shielded 'laser-flash' device (LAF-I) was designed and constructed at JRC-ITU for simultaneous measurement of the thermal diffusivity, $\alpha$, and heat capacity, $C_p$, of highly $\gamma$-active samples. These, in the form of a small disk or part of a disk, are heated up to a few tens of degrees below the measurement temperature in a high frequency furnace. Then a continuous-wave Y–Ar–Ga laser beam is used to further heat up the sample to the desired conditions, so that its brightness temperature is raised above that of the surrounding HF heater; this prevents the light emitted by the furnace from producing disturbing reflections on the sample surface. A laser pulse of 2 ms is finally applied to the front surface of the disk. The emerging temperature perturbation on the opposite surface is recorded by a photodiode-based pyrometer (0.05 K sensitivity) provided with a fast log-amplifier, and 14-bit A/D converter with a response time of the order of 10 μs. The recorded thermograms, $T = T(t)$, consisting of several thousands of points, are analysed by a realistic and accurate mathematical expression of the pulse propagation in the sample. The quantities $\alpha$ and $C_p$ are then calculated together with the occurring heat losses by a numerical fitting procedure followed by a self-consistency check of the resulting heat losses [2]. The precision of the $\alpha$ measurements is better than 5% and that of $C_p$ is of the order of 5–8%.

The experiments were carried out starting at 500 K with the aim of measuring $\alpha$ at increasing temperatures and of examining recovery effects, after laboratory thermal annealing above the fuel irradiation temperature. Thermal cycles were, therefore, applied corresponding to selected sequences of annealing temperatures ($T_{ann}$) up

Table 1
Irradiation temperature ($T_{irr}$, K), burn-up (bu, GWd t$^{-1}$) and density ($\rho$, kg dm$^{-3}$)

| Approx. burn-up GWd t$^{-1}$ | $T_{irr} \approx 750$ K | $T_{irr} \approx 900$ K | $T_{irr} \approx 1100$ K | $T_{irr} \approx 1450$ K |
|---|---|---|---|---|
| 0 | $\rho = 10.47$ | $\rho = 10.47$ | $\rho = 10.47$ | $\rho = 10.47$ |
| 34 | $T_{irr} = 730$<br>bu = 34<br>$\rho = 10.427$ | $T_{irr} = 860$<br>bu = 34<br>$\rho = 10.412$ | $T_{irr} = 1020$<br>bu = 33<br>$\rho = 10.419$ | $T_{irr} = 1210$<br>bu = 34<br>$\rho = 10.414$ |
| 52 | $T_{irr} = 680$<br>bu = 55<br>$\rho = 10.08$ | $T_{irr} = 890$<br>bu = 51<br>$\rho = 10.202$ | $T_{irr} = 1100$<br>bu = 51<br>$\rho = 10.174$ | $T_{irr} = 1300$<br>bu = 51<br>$\rho = 10.192$ |
| 76 | $T_{irr} = 700$<br>bu = 82<br>$\rho = 9.699$ | $\rho = 9.753$ | $\rho = 9.603$ | $\rho = 9.879$ |
| 92 | $T_{irr} = 730$<br>bu = 96<br>$\rho = 9.42$ | | | $T_{irr} = 1490$<br>bu = 92<br>$\rho = 9.699$ |

to ≈1450 K, a temperature at which one can observe that the radiation damage recovery processes are effectively completed, and substantial gas and volatile FP release takes place in concomitance with appreciable fuel swelling.

The thermal conductivity $\lambda(T)$ (in $\mathrm{W\,m^{-1}\,K^{-1}}$) was calculated from the independent measurement of the thermal diffusivity, $\alpha(T)$ (in $\mathrm{m^2\,s^{-1}}$), the heat capacity, $C_p(T)$ (in $\mathrm{J\,kg^{-1}\,K^{-1}}$), and the density $\rho(T)$ (in $\mathrm{kg\,m^{-3}}$). Since the analysis was to be focused on irradiation effects in the fuel lattice, thermal diffusivity changes due to macro-structural effects such as variation of the sintered porosity and fission gas swelling were considered as obvious, and *normalised* to 5% porosity by using the relation [3]:

$$\lambda_{95}(T) = \frac{1 - 0.05f(T)}{1 - Pf(T)}\alpha(T)\rho(T)C_p(T), \tag{1}$$

where $f(T) = 2.6 - 0.5T/1000$ and $P$ is the porosity fractional volume. In practice, the porosity of each sample was accurately measured by manual image analysis from scanned ceramographs and electron micrographs of several magnified images. In addition, the geometrical density was measured by a pycnometric technique at ambient temperature, whilst its temperature dependence was calculated from the thermal expansion coefficient recommended by Fink for fresh $UO_2$ [3].

### 2.3. Specific heat and thermal diffusivity

Classical measurements of the specific heat of irradiated fuel samples containing FP and lattice defects (in some cases frozen at super-saturated concentrations) would require a complex analysis of both the nature of possible $C_p$ components and of their implications in heat transport processes. Our measurement time was, however, so short compared with the occurring effective reaction/annealing rate of defects, and the applied laser probe pulse so weak, that a value of $C_p$ could be measured, which is representative for the instantaneous state of the sample. The results show that, at the explored temperatures, the magnitude of $C_p$ remains in the band of ±10% around the values corresponding to fresh fuel (Fig. 1). For the sake of brevity, the detailed measurements of $C_p$ are not discussed in this paper, where the specific heat of irradiated fuel was taken equal to that of the fresh $UO_2$ [3].

Indicative sets of thermal diffusivity measurements are shown in Fig. 2. The results, classified according to irradiation temperatures, can be summarised as follows (numerical values are given in Appendix A).

#### 2.3.1. Samples irradiated at ≈750 K

The measured thermal diffusivity decreases by approximately a factor of four in passing from the as-fabricated state to a burn-up of 100 $\mathrm{GWd\,t^{-1}}$ followed by a cooling time of 5–10 years. Only the low burn-up samples (35 $\mathrm{GWd\,t^{-1}}$) could be thermally annealed at sufficiently high temperatures to produce a clear (approximately 30%) recovery of the thermal diffusivity. The samples at burn-ups higher than 50 $\mathrm{GWd\,t^{-1}}$ disintegrated at temperatures, $T_{\mathrm{ann}}$, only slightly higher than $T_{\mathrm{irr}}$, and, consequently, no clear annealing effects on thermal diffusivity could be measured.

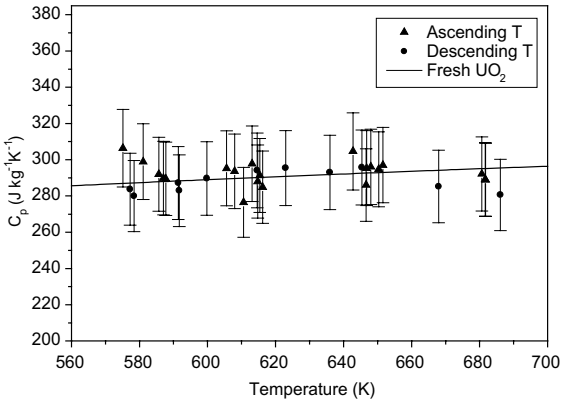


Fig. 1. Specific heat measurements for a sample irradiated at $T_{\mathrm{irr}} = 880$ K up to a burn-up of $\mathrm{bu} = 55$ $\mathrm{GWd\,t^{-1}}$.

#### 2.3.2. Samples irradiated at ≈1000 K

In low to medium burn-up samples (up to ≈50 $\mathrm{GWd\,t^{-1}}$), the effect of irradiation on the thermal diffusivity is clearly weaker than in the samples irradiated at 750 K. However, only the lower burn-up samples (35 $\mathrm{GWd\,t^{-1}}$) could be thermally annealed up to $T_{\mathrm{ann}} \approx 1450$ K. The annealing behaviour of $\alpha$ was analogous to that of samples irradiated at ≈750 K up to the same burn-up. The higher burn-up samples showed a better annealing endurance than the corresponding low $T_{\mathrm{irr}}$ samples. They also failed however after a thermal annealing at approximately 1200 K.

#### 2.3.3. Samples irradiated at ≈1100 K

The tendency of the post-irradiation thermal diffusivity to increase with the irradiation temperature was confirmed. The samples could be annealed up to 1450 K, temperature at which the diffusivity recovered approximately 15–20% of its initial value, and then failed.

#### 2.3.4. Samples irradiated at ≈1450 K

The thermal diffusivity is very close to that of other samples irradiated up to the same burn-up at lower temperatures, and annealed in the laboratory at $T_{\mathrm{ann}} = 1450$ K. Most samples broke as soon as the annealing temperature exceeded the in-pile value by a few tens of degrees. At sufficiently high temperatures, however, these measurements indicate that the curves of

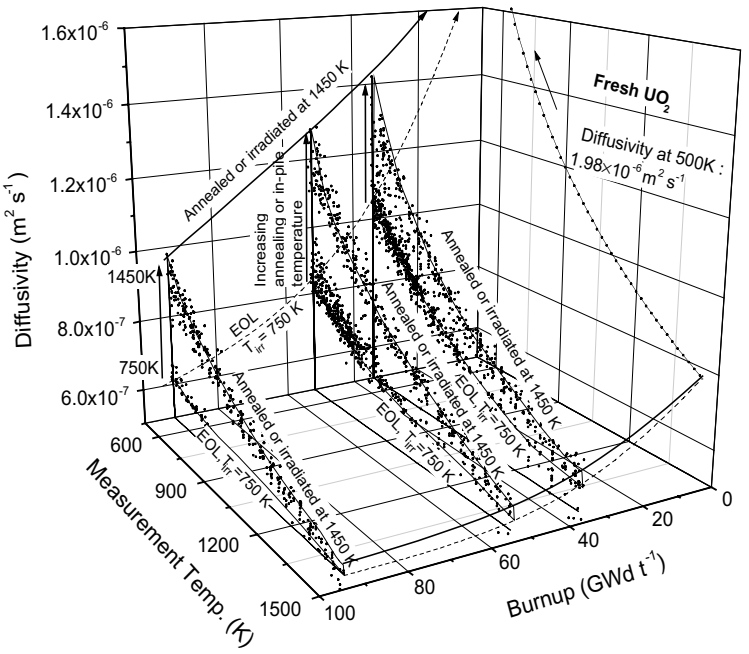


Fig. 2. Experimental thermal diffusivity of $UO_2$ as function of burn-up and irradiation temperature, before and after laboratory annealing (no porosity correction was applied).

$\alpha$ at end-of-life as a function of $T_{irr}$ and that of $\alpha$ as a function of $T_{ann}$ do effectively converge. The diffusivity of the high burn-up samples (100 GWd t$^{-1}$) is approximately 50% higher for samples irradiated at 1450 K compared to those irradiated at 750 K.

## 3. Modelling of thermal conductivity

In a crystal where heat is propagating through lattice vibrations only, the dependence of the thermal diffusivity on temperature, $T$, can be expressed by a simple relation of type $\alpha^{-1} = (a + bT)$. This property represents the most important prediction of first-order models of phonon/defect and phonon/phonon scattering [4]. It is plausible that these two mechanisms do actually govern heat transport in a poor semiconductor like $UO_2$ not only in the fresh state, but also after reactor-irradiation. In the former case, the experiment confirms this conjecture up to temperatures above 2500 K [4]. For the reactor-irradiated fuel, the inverse of thermal diffusivity was found to be sufficiently well described as a linear function of temperature provided that no major changes in the sintered structure take place (a log–log plot gives a slope of $0.99 \pm 0.02$). The slope, $b$, and the ordinate intercept, $a$, can therefore be tentatively analysed using the phonon scattering theory.

We briefly remind that, according to this simplest formulation of $\alpha^{-1}$, the ordinate intercept $a$ represents the effect of phonon-impurity scattering processes, and is expressed as

$$a = \frac{3}{\overline{V} \times \bar{\ell}}, \tag{2}$$

where vectors $\overline{V}$ and $\bar{\ell}$ are the average velocity and the mean free path of phonons along the considered direction, respectively. The latter can, therefore, be approximately expressed as

$$\langle \ell^{-1} \rangle = \left[ \sum_{k=1}^{\text{total}} \sigma_k N^k \right] = \langle \sigma \rangle N, \tag{3}$$

where $\sigma_k$ is the phonon cross-section of the scattering centres of type $k$, and $N_k$ their volume concentration. $N$ is the total impurity content and $\langle \sigma \rangle$ an effective scattering cross-section represented by some weighted average of the terms $\sigma_k$. Once the effect of radiation damage was suppressed by out-of-pile annealing, one should expect that the concentration of phonon scattering centres, that is related to the concentration of fission products, is a linear function of burn-up. Actually, until 100 GWd t$^{-1}$ the measured values of $a$ are reasonably well fitted by a straight line. Now, since the phonon velocity at our measurement temperatures is approximately constant ($4 \times 10^5$ cm/s), one can calculate from Eq. (2) the macroscopic scattering cross-section: the resulting cross-section radius is of the order of 0.4 nm, i.e., close to the U–U inter-distance in the f.c.c.

lattice. If one assumes this scattering cross-section also for FP impurities, one obtains an estimate of the concentration of scattering centres, as a function of burn-up. One can see that their concentration is almost equal to the fraction of fissioned uranium atoms. This means that, on the average, only approximately one half of the FP affects the vibrations of the atomic chains along which phonons propagate. The other half is accommodated or segregated in almost non-coherent or strain-free configurations, where the perturbations on the lattice interatomic potential are much weaker.

The temperature slope coefficient, $b$, is only dependent on the 'Umklapp' phonon–phonon scattering, the second important process producing resistance to thermal transport. All viable phonon scattering treatments agree in predicting that, above the Debye temperature, the thermal conductivity governed by this mechanism is inversely proportional to temperature, and expressed by the formula:

$$\lambda_u = \text{constant} \cdot \frac{Mn^{1/3}\delta\theta_D^3}{\gamma^2}\frac{1}{T} = \frac{C_v\rho}{bT} = \frac{1}{BT}, \tag{4}$$

where $M$ is the atomic mass, $\delta$ the average atomic size in the lattice unit cell containing $n$ atoms; $\rho$ is density, $\gamma$ is the Grüneisen coefficient and $\theta_D$ the Debye temperature.

It can be easily seen that in the investigated temperature range the magnitude of $B$ is effectively constant. If one considers the implied physical models (and also the mathematical approximations) leading to Eq. (4), one can realise that the *explicit* dependence of $\lambda_u^{-1}$ on temperature is a general prediction of statistical mechanics [5], provided that *implicit* temperature dependencies due to variation of the material properties with $T$ are not accounted for. The preceding considerations enable us to express also the thermal conductivity as $\lambda^{-1} = A + BT$, where $B$ and $A$ are, respectively, proportional to $b$ and $a$. In the following treatment the analysis will be concentrated on the coefficients $B$ and $A$. In particular, here the molecular volume is assumed to be constant. Now, experimental measurements of thermophysical properties are normally made under constant pressure conditions, since thermal dilation can hardly be countered. This problem is usually solved by substituting $C_p$ for $C_v$ in the proportionality factor between diffusivity and conductivity, and by introducing a correction of the effective sample dimensions at the measurement temperature. This procedure is only intuitive. However, there are no rigorous treatments to take into account thermal expansion. Formally, the volume dependence $z$ of $\lambda_u$ on $T$ can be deduced from Eq. (4):

$$z = -\left(\frac{\partial \ln(\lambda_u)}{\partial \ln(V)}\right)_T = 3\gamma - 1/3 + 2\left(\frac{\partial \ln(\gamma)}{\partial \ln(V)}\right)_T.$$

Thus, after introducing in Eq. (4) the temperature dependence of the molecular volume one obtains:

$$\lambda = \frac{\text{const.}}{T^{1+\varepsilon}} \quad \text{with} \quad \varepsilon = 3z\alpha_T T,$$

where $\alpha_T$ is the linear thermal expansion coefficient. Since in $UO_2$ we have $\gamma \approx 1.6$, the value of $z$ is larger than 4.5, and hence the temperature dependence of $\lambda_u$ on $1/T$ should significantly deviate from linearity – in disagreement with the experiment. Actually, the conductivity model leading to Eq. (4) is based on the assumption that the material properties are constant, so that this kind of extension should be considered with caution. The values of $b$ measured in fresh $UO_2$ and at low and medium burn-ups (<60 GWd t$^{-1}$) are not very different. At higher burn-ups, however, the value of $b$ decreases of approximately 20%. Though relatively few experimental points are available, their accuracy is sufficiently good to give credit to this observation. The cause of the decrease of $b$ can be conjectured from Eq. (4). Considering the expected magnitude of the physical quantities appearing in this equation, one should conclude that such a large variation can only be caused by a change of the Grüneisen constant $\gamma$, i.e., by the ratio of the isochoric thermal expansivity to the isothermal compressibility. There is one argument in favour of an increase of the compressibility at high burn-ups. In fact, our X-ray diffraction measurements indicate a slight decrease of the lattice parameter with burn-up (from the starting 0.5472 to 0.5468 nm at 100 GWd t$^{-1}$). However, if one considers that the major fission- and breeding-products, which are soluble in $UO_2$ and crystallise in the same group, have a significantly lower f.c.c. lattice parameter (e.g., $a_0(ZrO_2) = 0.507$ nm, $a_0(CeO_2) = 0.541$ nm, $a_0(PuO_2) = 0.5396$ nm), an ideal solid solution of urania with these elements, in a proportion of the order of 1 to 10, would produce a much larger lattice contraction than that reported above. This contraction is apparently hindered in the high burn-up fuel by the presence of other lattice defects – mostly Frenkel pairs and rare-gas atoms in interstitial sites – which are known to produce large lattice expansions. It is then plausible that the crystal submitted to these counterbalancing forces is more compressible than in their absence.

### 3.1. Model implementation

In the context of the preceding considerations and within the entailed restriction, the general expression of the heat conduction is also approximated by a similar formula:

$$\lambda = \frac{1}{A + BT}, \tag{5}$$

where $A$ and $B$ contain, as discussed above, all information on the heat capacity and on the most relevant phonon scattering processes. Most of the experimental measurements of the inverse thermal diffusivity versus

temperature could be well interpolated by straight lines whose coefficients were determined with sufficient precision to investigate their variation as a function of in-pile and annealing temperatures. An example of this analysis is shown in Fig. 3. Thus, starting from the obtained experimental database, a semi-empirical model for the thermal conductivity of the fuel was eventually deduced:

1. Firstly, the effect of defects that are *not* sensitive to thermal annealing was calculated from the measurements obtained at the maximal annealing temperature, i.e., at a temperature at which radiation damage displacements are absorbed by growing dislocation loops, voids and extended defects. The model parameters considered in this first class are therefore associated to the non-volatile FP and their compounds formed during irradiation (FP in lattice solution – which effect was analysed with the phonon scattering formulae, metallic and ceramic precipitates – which effect was analysed by using the theory of the effective conductivity of composite materials), and to the microstructure (porosity, cracks, and macroscopic irradiation defects not subject to anneal). Then the effect of gaseous and volatile FP present in a frozen atomic state was deduced from the experimental results by analysing the evolution of the conductivity during laboratory thermal annealing and for samples with and without rim restructuring.
2. The thermodynamic state of fission gas being not straightforward, the fraction of gas dynamically dissolved (gas-in-solid) and that precipitated (gas-in-bubbles) was predicted with a diffusion model calibrated with experimental results of ad hoc precipitation/release experiments carried out on representative irradiated fuel samples [6].
3. Furthermore, the contribution of radiation damage to the thermal conductivity deterioration was quantified from the measured magnitude and temperature dependence of the recovery process during laboratory thermal annealing. As the concentration of the lattice displacement defects is ruled by mechanisms (recombination, saturation, clustering, annealing) that are too complex to be viably formulated, their effect was empirically evaluated from the experiment.
4. Finally, the effect of out-of-pile self-irradiation was deduced from the behaviour of samples irradiated at high temperature, whose thermal conductivity decreased during storage, and begun to recover at laboratory annealing temperatures lower than the in-pile temperature.

In conclusion, a general parametric equation for the thermal conductivity of irradiated $UO_2$ was obtained. Based on this equation, an iterative computer model was constructed, applicable to complex irradiation histories. Its predictions are compared in the last section of this paper with those based on the Halden correlation [7].

### 3.2. General expression for the effect of fission products

Formula $\lambda = \frac{1}{A+BT}$ was successfully applied in the past to describe the variation of the lattice thermal conductivity of $UO_2$ due to addition of one, or a few, FP with molar fractions up to about 20% [8]. Since at the considered highest burn-up the total molar fraction of FP soluble in $UO_2$ is less than 10%, the same model can be applied to all soluble FP, starting from available

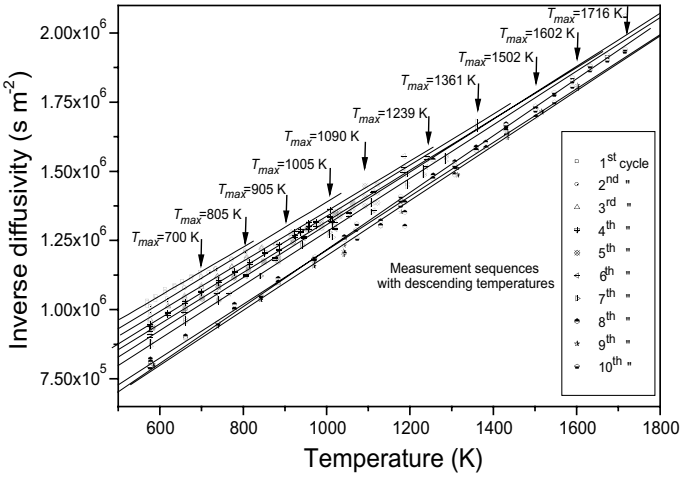


Fig. 3. Inverse thermal diffusivity measured in a LWR $UO_2$ sample irradiated to 30 GWd t$^{-1}$ at an in-pile temperature of approximately 800 K, and submitted in laboratory to a sequence of thermal annealing cycles, the peak temperatures of which are indicated in the plot by vertical arrows.

information on their chemical and physical state in the matrix.

The fuel matrix is described as a solid solution where the components may have widely different lattice radii, which can be calculated from the cell parameter of the correspondent (di)oxide crystal. The lattice is thus supposed to contain strained regions acting as phonon scattering centres, whose cross-sections can be calculated from the geometrical property of the local impurity. The effect is similar for dimensionally conform impurities but which have a mass different from that of the substituted atoms.

The constant $A$ can be expressed as the sum of the thermal resistance due to phonon scattering by individual point defects (interstitial atoms, vacancies, impurities), as well as dislocations and extended defects. Ambegaoker [9] obtained the following relation:

$$A = \frac{\pi^2 \overline{V} \theta_D}{3\bar{v}^2 h} \sum_i \Gamma_i = C \sum_i \Gamma_i, \tag{6}$$

where $\overline{V}$ is the mean atomic volume of the lattice, $\theta_D$ the Debye temperature, $\bar{v}$ the mean phonon velocity, $h$ Planck's constant, $\Gamma_i$ the phonon diffusion cross-section of defect $i$. In the present study, the values of $\Gamma_i$ were calculated, whilst the constant $C$ was taken as unit in agreement with the literature data [10–13]. The parameter $\Gamma_i$ depends on the local perturbation in mass, strain and bonding potential brought about by the point defect of type '$i$' in the host lattice. The total scattering coefficient has the approximate expression [14]:

$$\begin{aligned}\Gamma &= \sum_i \Gamma_i = \sum_i y_i \left[ \left( \frac{\overline{M} - M_i}{\overline{M}} \right)^2 + \varepsilon \left( \frac{\bar{r} - r_i}{\bar{r}} \right)^2 \right] \\ &= \left( \frac{\sum x_i M_i^2 - \overline{M}^2}{\overline{M}^2} \right) + \varepsilon \left( \frac{\sum x_i r_i - \bar{r}^2}{\bar{r}^2} \right),\end{aligned} \tag{7}$$

where $y_i$ is the atomic partial fraction of point defect $i$, $M_i$ its atomic weight, and $r_i$ its ionic radius. $\overline{M}$ is the mean atomic mass and $\bar{r}$ the mean ionic radius of the lattice. The constant $\varepsilon = 32(1 + 1.6\gamma)^2$ – where $\gamma$ is the Grüneisen constant – represents the strain generated in the lattice by the ionic radius difference, and is usually treated as an empirical parameter obtained from experimental data [15]. In the present study, $\varepsilon$ was fixed to 100 in agreement with the literature data for solid solutions of two actinides oxides [10–12,15–17] or containing a large number of actinides [8,11].

The product $BT$ corresponds to the intrinsic lattice thermal resistivity caused by phonon–phonon scattering. The value of $B$ can be evaluated from a simplified model [18] resulting in the relation:

$$B = \frac{\gamma^2}{\frac{24}{10} 4^{1/3} \left( \frac{h}{k} \right)^3 \overline{M}\, \overline{V}^{1/3} \theta_D^{1/3}}, \tag{8}$$

where $k$ is the Boltzmann constant. The variation of the elastic constants in irradiated fuel is still under investigation in our laboratory. However, evaluation of Eq. (8) from physical and thermodynamic data of $UO_2$ data is not sufficiently accurate to validate the model, and, a fortiori, to predict the evolution of $B$ with burn-up and irradiation temperature. Therefore, $B$ was empirically obtained from a fitting of the measured thermal resistivity slopes.

### 3.3. Inventory, chemical state and effect of fission products

The FP concentrations were calculated with the ORIGEN 2 code [19], by using appropriate fission-yield databases, for the appropriate reactor, fuel enrichment and burn-up examined. The calculated concentrations of a few selected nuclides were confirmed by mass spectrometric analysis. The chemical state of the individual elements was assessed based on their effective solubility in the fuel matrix [20], namely:

1. Actinides, rare earths and transition metals were assumed to form mixed oxides with $UO_2$. As their solubility limits determined for binary systems are never reached in the case of FP, it was supposed that the following elements are completely dissolved in the fuel: Nd, Zr, Ce, Pu, Ba, La, Pr, Sr, Sm, Y, Rb, Te, Np, Pm, Eu, Gd, Am, Th, Cm, Nb, Pa.
2. Kr and Xe were assumed to be present either as a *dynamically dissolved* phase in the fuel lattice (see below), or precipitated as gases in intra- and intergranular bubbles or open porosity (or released to the plenum). Cs was assumed to be in part dissolved in the matrix, in part trapped as a fluid in bubbles and closed pores, and in part precipitated in solid compounds (see below). Other volatile FP, like Br and I, were treated in a similar manner.
3. Oxides like $BaZrO_3$ or $SrZrO_3$, insoluble in the matrix, as well as more volatile compounds like CsI, and $Cs_2MoO_4$ have been taken into account as ceramic precipitates.
4. Also separately treated were the FP of the platinoid group together with some other elements (Mo, Ru, Tc, Rh, Te, Pd, Sn, Cd, Sb, Ag, In), which were considered as metallic phases.

The calculation of the total scattering parameter $\Gamma$ was performed for all soluble FP, volatile and non-volatile, listed in points (1) and (2); the data used are reported in Appendix B. The value of $\Gamma$ was found to depend linearly both on the amount of dissolved FP, that is proportional to burn-up, and on the amount of

dynamically dissolved volatile FP, that is proportional to the product bu GIS, where GIS is the fraction of gas-in-solid defined as the ratio of the gas amount present in dynamical solution to the total produced inventory. The obtained values of $A$ (Eq. (6)) were then compared to the measured ones (Fig. 8).

Some remarks must be made concerning the method of analysis of these results:

The value of $A$ after annealing depends not only on the amount of FP dissolved in the fuel matrix, but also on metallic or ceramic precipitates listed in points (3) and (4). The effect of the former on the conductivity was evaluated by using the Maxwell–Eucken equation predicting the effective conductivity of a matrix containing different kinds of inclusions [21]; this formalism is in fact adequate for the small volume fractions considered. The inventory of the FP metallic precipitates is given in Appendix B. The volume fraction of each constituent was evaluated from the number of moles created supposing a density of 10 $\mathrm{g\,cm^{-3}}$. Then the Maxwell–Eucken formula was applied using the annealed value of the thermal conductivity for the matrix, and a conductivity of 100 $\mathrm{W\,m^{-1}\,K^{-1}}$ for all the metallic inclusions. The effect of the metallic inclusions is to improve the effective conductivity with increasing burn-up, the gain being of 5.8% at 90 $\mathrm{GWd\,t^{-1}}$ burn-up. The effect is little sensitive to the adopted value of the conductivity of the metallic phase. For instance, if the inclusions are supposed to have a conductivity of 50 $\mathrm{W\,m^{-1}\,K^{-1}}$, the increase is of 5.4% instead of 5.8%. The FP ceramic precipitates are supposed to have conductivities of magnitudes near or lower than that of $UO_2$ (see, e.g., the work of Krishnaiah on some rare earth-uranium ternary oxides [22]). A detailed inventory of these precipitates is unnecessary because their effect on the total conductivity is much smaller than that of the metallic inclusions. Finally, the two antagonist effects on $A$ of metallic and ceramic precipitates depend linearly on burn-up, and not on in-pile or annealing temperatures, and for this reason they cannot be distinguished from the one of the dissolved fission products. For simplicity purposes, the Maxwell–Eucken formula was not introduced in the model and the effect was included in the term proportional to bu in Eq. (9).

The effect of the elements listed in points (1), (3) and (4) was first quantified by analysing the curves obtained after laboratory annealing. This corresponds to changes in $A$ measured in samples where the lattice displacement damage has been completely annealed out, and volatile FP are precipitated or released, i.e., GIS = 0. The calculated values of $A$ were compared to the experimental curve on Fig. 8 labelled 'annealed at 1450 K'.

Among the elements listed in (1), the substitutional impurities Rb, Ba and Sr have a very large impact on $\Gamma$, for instance, the strong negative effect of Ba is consistent with the measured thermal conductivity of $BaUO_3$, which is about one tenth of that of $UO_2$ [23]. Since data on their solubility in $UO_2$ are lacking, a dissolved fraction of 24% of the inventory was assumed in order to obtain agreement with the experiment; the remaining quantity was, therefore, supposed to form ceramic precipitates.

The effect of dynamically dissolved Xe and Kr and other volatile FP listed in point (2), as calculated from their atomic radius, is comparatively high. Actually, the possible lattice defect configurations of gas-in-solid (e.g., association to a Schottky trio) would require a more complex treatment than that leading to Eq. (6). In practice, an empirical factor had do be applied in order to reproduce the observed effect of gas-in-solid on $A$ (Eq. (9)) by analysing the value of $A$ before and after the rim formation, where GIS decreases from $\approx 1$ to $\approx 0$ (curve labelled '$T_{\mathrm{irr}} = 750$ K' on Fig. 8).

Finally, the obtained expression has the form:

$$\Gamma(\mathrm{bu},\ \mathrm{GIS}) = 9.02 \times 10^{-4}\ \mathrm{bu}\ \mathrm{GIS} + 1.74 \times 10^{-3}\ \mathrm{bu} + 7.51 \times 10^{-3}, \tag{9}$$

where bu is the local fuel burn-up (in $\mathrm{GWd\,t^{-1}}$).

As GIS is an important parameter in the expression of $\Gamma$, its evaluation is discussed in some detail the next section. Other parameters concerning the fuel chemical composition are not examined here, for instance, the fuel is supposed stoichiometric. The effect on the scattering parameter of an eventual oxygen non-stoichiometry can be evaluated by the same formalism [10].

### 3.4. Model for the physical state of volatile fission products

The behaviour of fission gas retained in the fuel at end-of-life (EOL) was calculated with a computer code for each irradiation temperature and burn-up. Due to the variation of structural parameters like pore size (Fig. 4) and grain size during irradiation, a numerical calculation covering the entire life of fuel in reactor was carried out. Then, the expression of the GIS variable was calculated using a gas diffusion/precipitation/release model (see Appendix C). The numerical integrals of the rate equations require long calculation time. We have, therefore, carried out a set of parametric evaluations of GIS, and found an interpolating spline function that provides a sufficiently precise fitting of GIS for evaluating Eq. (9). The approximate expression is

$$\mathrm{GIS}(\mathrm{bu}, T_{\mathrm{irr}}, T_{\mathrm{ann}}) = \frac{1 - 0.9\left[1+\exp\left(\frac{T_{\mathrm{irr}}-950}{30}\right)\right]^{-1}\left[1+\exp\left(\frac{73-\mathrm{bu}}{2}\right)\right]^{-1}}{\left[1+\exp\left(\frac{T_{\mathrm{irr}}-1350}{200}\right)\right]\left[1+\exp\left(\frac{T_{\mathrm{ann}}-1350}{200}\right)\right]}. \tag{10}$$

The values obtained with this function of burn-up, irradiation and annealing temperatures are compared

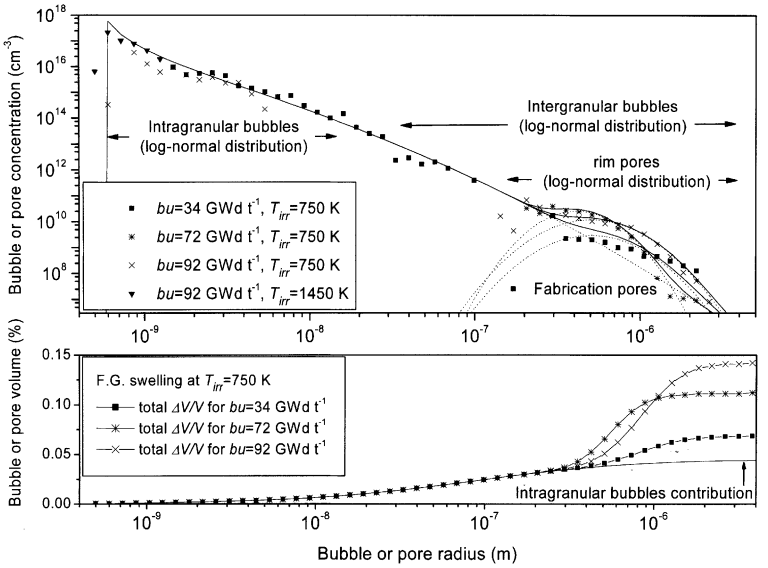


Fig. 4. Bubble and pore size distributions (measured by image analysis and interpolated by log-normal distributions) and contribution of the different populations to the voids volume fraction. A coefficient $k_{sc}^2 = 4.1 \times 10^{11}$ (m$^{-2}$) was calculated from the plotted distribution.

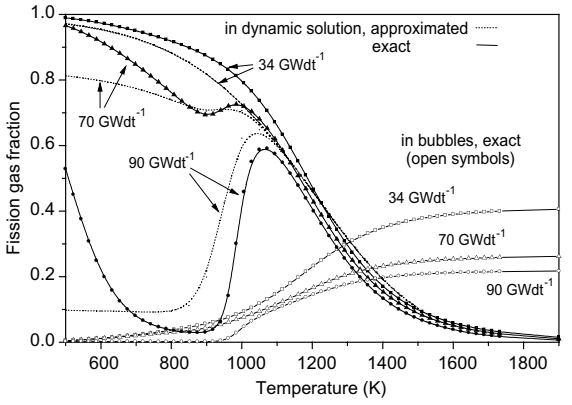


Fig. 5. Calculated fission gas fractions in dynamic solution and in intra-granular bubbles for different burn-ups and as functions of irradiation temperature (irradiation time is the same for all burn-ups, different burn-ups were obtained with different irradiation powers).

with the calculated values (using Eq. (C.3), Appendix C) in Fig. 5. Note that the second bracket on the numerator describes the diminution of GIS as the rim structure is gradually formed (high burn-ups at low $T_{irr}$). The change of GIS during a post-irradiation annealing at $T_{ann} > T_{irr}$ is also taken into account in the second denominator factor.

### 3.5. Behaviour of irradiation defects in thermal annealing cycles

The concentration of point defects due to radiation damage (Frenkel-pairs and their clusters) depends on temperature only, since their saturation occurs at much lower *dpa*'s than those achieved at the considered burn-ups. In contrast, the concentration of dislocations and extended defects depends both on temperature and burn-up and increases with burn-up, because point defects are continuously aggregating after reaching the saturation level. The effect of these defects on the conductivity was deduced from the results obtained during the annealing cycles. It is supposed that the thermal conductivity values converge, *after complete annealing*, to the same value for all samples having the same burn-up, independent of their irradiation history. However, it should be remarked that this property could not be completely proved experimentally, since most samples irradiated at low temperatures disintegrated during the laboratory thermal treatment before reaching complete annealing.

#### 3.5.1. Variation of coefficient A

*(i) Out-of-pile self-irradiation effect as determined by low temperature annealing*

During laboratory annealing, the samples irradiated between 800 and 1200 K in addition to a stronger recovery at temperatures higher than $T_{irr}$, showed a moderate recovery even at temperatures lower than $T_{irr}$. Furthermore, also samples irradiated at high temperature (1450 K), where the in-pile concentration of irradiation point defects is low, exhibit a thermal conductivity recovery at $T < T_{irr}$. The variation of $A$ at temperatures below $T_{irr}$ is of the order of $\approx 0.02$ m K W$^{-1}$. This recovery corresponds to healing of self-irradiation defects produced between EOL and the time

of the measurements (in most cases a few years). This self-irradiation effect is supposed to be present in all samples, independently of the irradiation temperature and burn-up. This means that the values of $A$ at EOL were always slightly lower than those measured in laboratory, and a compensation was to be applied.

Within the uncertainty limits, the recovery of the self-irradiation effect was found to be proportional to the annealing temperature in the range from 900 to 1450 K. In order to obtain a formula also valid for fresh fuel, a factor weakening this effect as bu decreases was introduced ($F(\mathrm{bu})$, see below). Therefore, the value of $A$ due to out-of-pile self-irradiation as a function of burn-up (bu in GWd t$^{-1}$) and temperature, $\delta A_{\mathrm{Self}}$, was fitted by an empirical function:

$$F(\mathrm{bu}) = \left(\left(1+\exp\left(\frac{20-\mathrm{bu}}{6}\right)\right)^{-1} - 0.015267\right), \tag{11}$$

$$\delta A_{\mathrm{Self}}(T_{\mathrm{ann}}, \mathrm{bu}) = \begin{cases} 0.02F(\mathrm{bu}) & \text{if } T_{\mathrm{ann}} \leqslant 900 \text{ K}, \\ 0.02F(\mathrm{bu})\frac{1450-T_{\mathrm{ann}}}{1450-900} & \\ \quad \text{if } 1450 \text{ K} > T_{\mathrm{ann}} > 900 \text{ K} & \text{in m K W}^{-1}, \\ 0 & \text{if } T_{\mathrm{ann}} \geqslant 1450 \text{ K}. \end{cases} \tag{12}$$

*(ii) In-pile damage effect*

After subtracting the out-of-pile auto-irradiation effect, samples with low burn-up and low $T_{\mathrm{irr}}$ (e.g., 35 GWd t$^{-1}$, 750 K) showed a conductivity recovery in the form of a decrease of the coefficient $A$ at temperatures higher than approximately 900 K (Fig. 6). The recovery was progressive until the maximum annealing temperature (1450 K). A closer observation of the curve of Fig. 6 reveals different stages characterised by: (i) no recovery between 650 and 800 K, (ii) a progressive, slow recovery between 800 and 1000 K, (iii) no further recovery until 1200 K, and (iv) further recovery until 1350 K. The variation of $A$ due to the effective concentration of irradiation defects at EOL, $\delta A_{\mathrm{EOL}}$, was investigated for different burn-ups (Fig. 7) and was be expressed as

$$\delta A_{\mathrm{EOL}}(T_m, \mathrm{bu}) = \frac{\mathrm{bu}}{850}\left[\left(1+\exp\left(\frac{T_m-950}{25}\right)\right)^{-1} + \left(1+\exp\left(\frac{T_m-1300}{35}\right)\right)^{-1} - 0.0525\right] \text{ in m K W}^{-1} \tag{13}$$

with $T_m = \max(T_{\mathrm{irr}}, T_{\mathrm{ann}})$. The formula is validated in the temperature range from $T_{\mathrm{irr}}$ to 1450 K.

Consistently with the experimental results presented in Fig. 8, for a given temperature, the effect of in-pile and out-of-pile thermal annealing of irradiation defects is equivalent, so that $\delta A_{\mathrm{EOL}}(T_{\mathrm{irr}}, \mathrm{bu})$ is calculated by the same function, replacing $T_{\mathrm{irr}}$ by $T_{\mathrm{ann}}$ when $T_{\mathrm{ann}} > T_{\mathrm{irr}}$.

*3.5.2. Variation of coefficient B*

The observed variation of the coefficient $B$ at EOL and after annealing is opposite to that of $A$ (Fig. 6). The effect of annealing of irradiation defects existing at EOL is plotted in Fig. 7 for different burn-ups. The variations of $B$ with temperature and burn-up, $\delta B_{\mathrm{EOL}}$, are fitted by the function:

$$\delta B_{\mathrm{EOL}}(T_m, \mathrm{bu}) = \frac{\mathrm{bu}}{34}\left[4.0\times10^{-5}\left(1+\exp\left(\frac{T_m-950}{25}\right)\right)^{-1} + 2.5\times10^{-5}\left(1+\exp\left(\frac{T_m-1300}{35}\right)\right)^{-1}\right] \text{ in m W}^{-1} \tag{14}$$

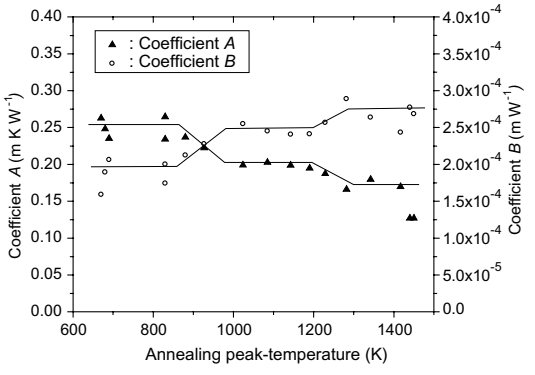


Fig. 6. Effect of the maximum annealing temperature on $A$ and $B$ coefficients for a sample with bu = 35 GWd t$^{-1}$ and $T_{\mathrm{irr}}$ = 750 K.

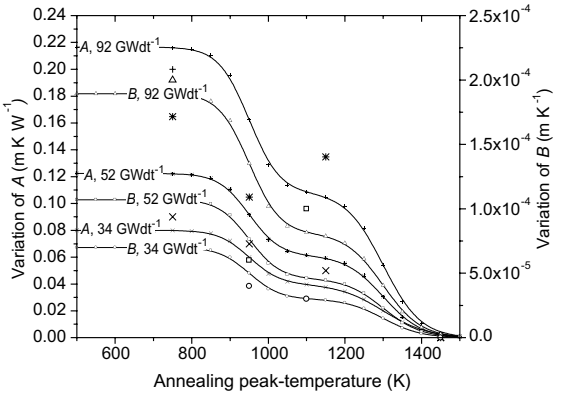


Fig. 7. Effect of irradiation defects present at EOL as a function of irradiation temperature, expressed as the variation of $A$ (decrease) and $B$ (increase) during out-of-pile annealing (calculated: small symbols and curves, experimental: big symbols).

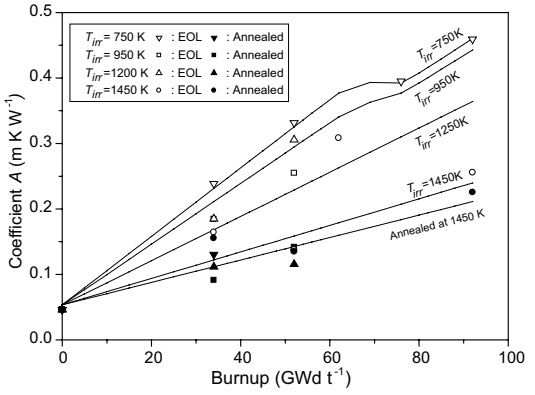


Fig. 8. Predicted value of coefficient $A$ as a function of burn-up compared with experiment.

with $T_m = \max(T_{\rm irr}, T_{\rm ann})$. The temperature application range is the same as for $A$.

### 3.6. Complete formula for the thermal conductivity

In conclusion, the adopted thermal conductivity expression interpolates the combined effects of burn-up, irradiation and post-irradiation temperature history. In order to obtain a formula of general applicability, parameters have been included and evaluated, which account for the effect of:

(i) soluble, non-volatile fission products,
(ii) fission gas and Cs content and its state (also accounting for the effect of rim restructuring),
(iii) irradiation defects (both present at EOL and created during subsequent storage by self-irradiation), and, for thermal recovery conditions:
(iv) precipitation of the fission gas-in-solid, and
(v) annihilation of irradiation defects.

The thermal conductivity (normalised to 5 vol.% fabrication porosity) is finally expressed by maintaining the original simple formula for phonon scattering, with, however, variable coefficients $A$ and $B$:

$$\lambda = [A(T_{\rm irr}, T_{\rm ann}, {\rm bu}) + B(T_{\rm irr}, T_{\rm ann}, {\rm bu})T]^{-1}, \qquad (15)$$

where:

- $T$: instant application temperature (300–1500 K);
- $T_{\rm irr}$: irradiation temperature (700–1450 K);
- $T_{\rm ann}$: maximum temperature (700–1450 K) reached during annealing following irradiation at $T_{\rm irr}$;
- bu: burn-up (0–100 GWd t$^{-1}$).

(i) The coefficient $A$ is given by

$$A(T_{\rm irr}, T_{\rm ann}, {\rm bu}) = 0.046 + \Gamma({\rm bu}, {\rm GIS}) + \delta A. \qquad (16)$$

In this equation, the figure 0.046 is the value of $A$, measured in the same $UO_2$ fuel pellets before reactor-irradiation. This value is completely independent of the irradiation effects, and may be adjusted if a fuel with a different starting thermal conductivity is considered. The second term on the right hand side represents the phonon scattering from FP, separated in soluble and volatile/insoluble ones. The third term is due to radiation damage, subdivided in in-pile damage and self-irradiation damage.

The impurity/phonon scattering coefficient, $\Gamma({\rm bu}, {\rm GIS})$, is given by Eq. (9) and GIS, the concentration of fission gas frozen in dynamical solution at EOL, is approximated by Eq. (10).

The effect of the irradiation defects on $A$ is defined as a function of $T_m = \max(T_{\rm irr}, T_{\rm ann})$:

$$\delta A = \delta A_{\rm Self}(T_m, {\rm bu}) + \delta A_{\rm EOL}(T_m, {\rm bu}), \qquad (17)$$

where the two terms at the right hand side are given by Eqs. (12) and (13), respectively.

(ii) The evolution of the coefficient $B$ was analysed with the same methodology and was interpolated from experimental measurements (Fig. 9) by

$$B(T_{\rm irr}, T_{\rm ann}, {\rm bu}) = B_0 + (B_1 - B_0)\frac{(6.5\times10^{-5} - \delta B)}{6.5\times10^{-5}}. \qquad (18)$$

The values of $B$ at EOL ($B_0$) and after total annealing at 1450 K ($B_1$) deduced from Fig. 9 were interpolated by straight lines:

$$B_0 = -1.65\times10^{-6}\ {\rm bu} + 2.55\times10^{-4} - 3.6\times10^{-5}\ {\rm IRIM\ in\ m\,W^{-1}} \qquad (19)$$

with a correction associated to the rim formation having a maximal amplitude of $3.6\times10^{-5}$ m W$^{-1}$ (deduced from the curve labelled '$T_{\rm irr} = 750$ K' on

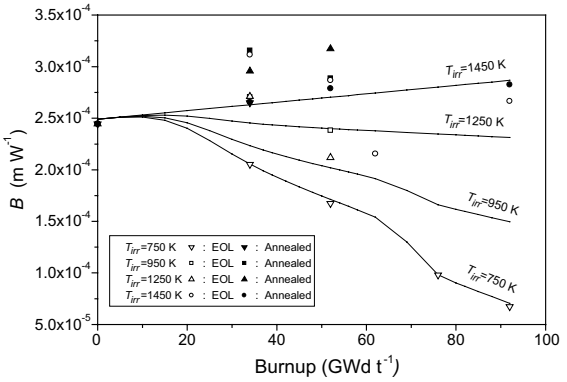


Fig. 9. Predicted value of coefficient $B$ as function of burn-up compared with experiment.

Fig. 9) and a bu and $T_{irr}$ dependence similar to the one proposed for the GIS variable (Eq. (10)):

$$\mathrm{IRIM} = \left[1 + \exp\left(\frac{T_{irr} - 950}{30}\right)\right]^{-1} \times \left[1 + \exp\left(\frac{73 - \mathrm{bu}}{2}\right)\right]^{-1} \quad (20)$$

and

$$B_1 = 4.2 \times 10^{-7}\ \mathrm{bu} + 2.75 \times 10^{-4}. \quad (21)$$

The effect of the irradiation defects on the value of $B$ is separately expressed as follows:

$$\delta B = F(\mathrm{bu})\delta B_{\mathrm{EOL}}(T_m, \mathrm{bu}), \quad (22)$$

where $F(\mathrm{bu})$ is given by Eq. (11), $\delta B_{\mathrm{EOL}}(T_m, \mathrm{bu})$ is given by Eq. (14) and $T_m = \max(T_{irr}, T_{ann})$. As for the $A$ coefficient, the factor $F(\mathrm{bu})$ was introduced in order to extrapolate the formula to fresh fuel.

The experimental and predicted values of the coefficients $A$ and $B$ are plotted in Figs. 8 and 9, respectively. The predicted thermal conductivity is plotted in Fig. 10 and the numerical values are presented in Appendix A with the experimental results. The agreement, before, during and after annealing, is better than 5% for almost all the samples.

Some features are particularly noteworthy:

- The effect of rim restructuring, which entails a significant decrease in the fission-gas concentration dynamically dissolved in the matrix, can be clearly seen in the graphs: the thermal conductivity at EOL, plotted in Fig. 11 as a function of irradiation temperature for different values of burn-up, shows that the formation of the rim structure has a *positive* effect on the *lattice* thermal conductivity (i.e., if the trivial diminution due to fission-gas swelling is not taken into account). This effect has already been anticipated by Spino and Papaioannou [24] from the analysis of the lattice parameter during the rim formation.
- Fig. 12 shows the evolution with burn-up of the conductivity measured at 900 K, for different irradiation temperatures, normalised to 5% porosity. It can be seen that the samples displaying the rim structure have higher lattice conductivity than those irradiated at about 1200 K, a temperature at which the rim structure is *not* formed. One can see that only in samples irradiated at $T_{irr} > 1500$ K does the lattice conductivity become higher than that measured in the rim structure.
- Finally, the value of $B$ decreases by a factor of five in samples which exhibit rim restructuring. If $B$ is interpreted on the basis of Eq. (8), the only physical

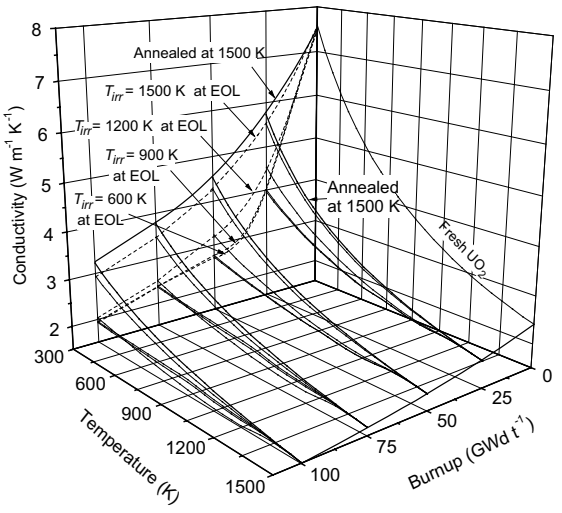


Fig. 10. Thermal conductivity of $UO_2$ as a function of temperature, for irradiation temperatures of 600, 900, 1200 and 1500 K, at EOL and after out-of pile annealing up to 1500 K.

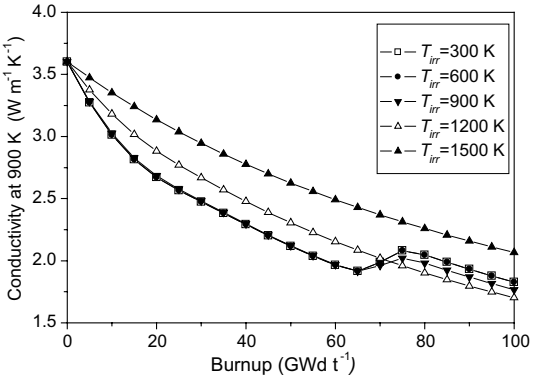


Fig. 11. Calculated thermal conductivity at EOL as a function of irradiation temperature, for different burn-ups.

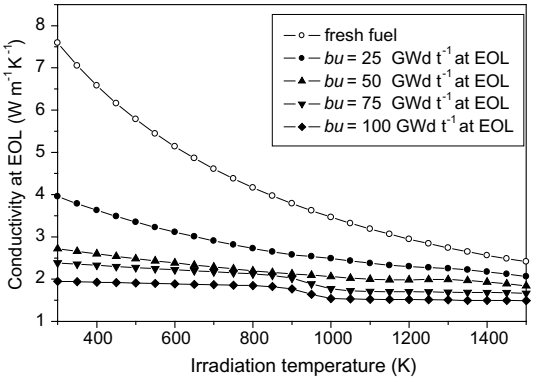


Fig. 12. Calculated thermal conductivity at 900 K as a function of burn-up, for different irradiation temperatures.

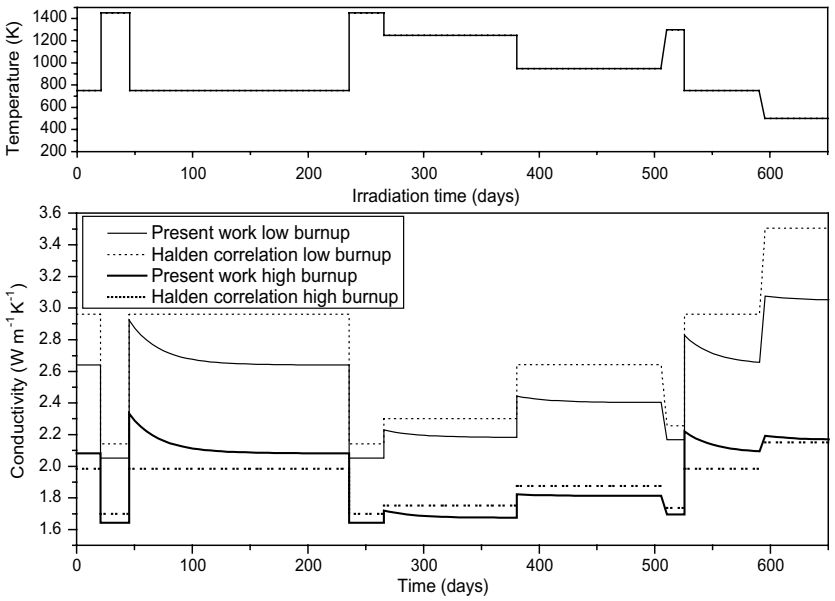


Fig. 13. Thermal conductivity of $UO_2$ calculated by the present model for a complex power history at burn-ups of, respectively, 35 and 90 GWd t$^{-1}$, and compared with that of the Halden correlation.

quantity appearing in this formula which can realistically undergo a proportionate change is the Grüneisen constant, $\gamma$ (which, to produce the observed effect on $B$, should decrease by approximately a factor of two). If in turn we consider the definition of $\gamma$, we realise that the change can only be produced by a proportional decrease of the isothermal compressibility of the lattice. Since, however, this interpretation is so far only conjectural, the issue might merit further investigation.

### 3.7. Extension of the model to complex irradiation histories

The in-pile temperature evolution of fuel submitted to real power histories is usually irregular, and it is hardly possible to define an effective $T_{irr}$ value from which the instant thermal conductivity can be calculated.

In order to account for irradiation conditions, a time-dependent recovery of the thermal conductivity was introduced. It was supposed that recovery is instantaneous when temperature is increased. This is consistent with our experimental results, for which the total annealing time at high temperatures was of the order of 15 min, and no further measurable recovery was obtained for annealing times of about 1 h.

In contrast, when $T_{irr}$ is decreased, the radiation damage cannot instantly achieve the steady state concentration. At a fission rate of the order of $10^{13}$ cm$^{-3}$ s$^{-1}$ it was assumed that steady state is reached after approximately 100 days irradiation. To account for this effect in the computer programme, the number of irradiation defects present in the fuel was stored between subsequent time steps. This was made by recording at each calculation step the values of the constants $A$ and $B$ (or $\delta A$ and $\delta B$), and by evaluating their variation during the time elapsed.

The evolution of the thermal conductivity for a typical segment of a LWR power history is plotted in Fig. 13, and is compared with the predictions obtained by the Halden correlation ($T$ in °C) [7]:

$$\lambda = \frac{1}{0.1148 + 0.0035\ \text{bu} + (0.0002474 - 8.24 \times 10^{-7}\ \text{bu})T + 0.0132\exp(0.00188T)}\ \text{in W m}^{-1}\,\text{K}^{-1}.$$

The local fuel temperature was varied between 750 and 1450 K and two burn-ups were considered: 35 and 90 GWd t$^{-1}$. Actually, it should be noted that only the values *after* recovery can be compared, because transients are *not* taken into account by the Halden correlation.

It can be seen that the maximum discrepancy between the results is less than 5% at 90 GWd t$^{-1}$, but at 35 GWd t$^{-1}$ the values predicted by the Halden correlation are up to 10% higher than those presented here.

## 4. Conclusions

The thermal diffusivity and the heat capacity of irradiated $UO_2$ fuels were measured, and laboratory

thermal annealing cycles with increasing maximum temperatures were applied to examine recovery effects.

The measured heat capacity of irradiated fuel remains in the band ±10% around the values corresponding to fresh fuel, so that the marked deterioration of the thermal conductivity, $\lambda$, with burn-up is mainly due to a decrease of the thermal diffusivity.

The decrease in conductivity due to swelling caused by fission gas bubbles was considered as an extrinsic effect, which can be accounted for in terms of a conventional correction for a porous medium. All experimental data were, therefore, referred to a standard as-fabricated pellet with a density of 95% of the theoretical density.

The most conspicuous decrease in diffusivity was observed in high burn-up samples subjected to in-pile temperatures of 600–800 K. These samples showed a decrease in conductivity of up to a factor of four compared to fresh fuel.

Analysis of the experimental measurements shows that the effective decrease of $\lambda$ during reactor-irradiation is due to: (a) atomically dispersed FP, (b) irradiation and self-irradiation defects, (c) fission gas and volatile FP dynamically frozen in the fuel during irradiation, (d) fission gas precipitation and porosity evolution.

The important effects due to fission gas are interpreted by considering the possible states, from gas-in-solid through bubble precipitation until inter-granular swelling conditions. These aspects were investigated both experimentally (electron microscopy, gas release under thermal annealing with on-line mass-spectrometric measurements), and with the help of fission gas diffusion models.

Thermal annealing leads to defect annihilation, and to healing of the lattice with a consequent recovery of thermal diffusivity. The recovering effects after laboratory annealing at a given temperature are similar to those measured at EOL in samples irradiated at the same temperature. However, with the increase of burn-up, large stresses are produced in the matrix during laboratory annealing with sudden development of cracks. The higher is the fuel burn-up, the lower the temperature at which these processes are activated. At 100 GWd t$^{-1}$ the fuel disintegrates at temperatures just above the in-pile temperature. Therefore, a prediction of the thermal transport performance of the outer pellet region of high burn-up fuel (which exhibit the characteristic rim structure) under transient conditions is still uncertain, and further measurements must be conducted where $\lambda$ is measured under restrained conditions.

Finally, the formation of the typical rim structure has a positive effect by limiting the decrease in $\lambda$ with burn-up. It is remarkable that, for temperatures below $T_{irr}$, the slope, $B$, of the thermal resistivity $\lambda^{-1} = A + BT$ is lower in the rim zone. According to the current phonon scattering theory this should imply some sort of 'softening' of the matrix.

## Acknowledgements

The authors would like to thank the HBRP Steering Committee for permitting publication of some of their data produced during a multi-annual irradiation and post-irradiation examinations campaign. We gratefully acknowledge the invaluable contribution of the ITU Thermophysics Laboratory staff: Dave Halton, Mauro Martellenghi, Giorgio Pagliosa and Mike Joergensen. Furthermore, this complex work was made possible by the collaboration of a number of persons who, with patience and skill, prepared the samples and managed the characterisation and post-irradiation examinations of the selected fuels. Therefore, we should like to thank the Head of the Hot Cell Unit of ITU, J.P. Glatz, and, in particular, D.P. Bottomley and V.V. Rondinella. Finally, a number of unpublished results have been used in this paper which have been kindly made available by the Electron Microscopy (T. Wiss) and Thermodynamics (J.P. Hiernaut) Laboratories of ITU.

## Appendix A. Experimental and calculated values of thermal conductivity

Experimental and calculated values of thermal conductivity $\lambda$ for burn-ups of 34, 52, 82 and 92 GWd t$^{-1}$ and different irradiation temperatures, before and after laboratory annealing (normalised to 5% porosity) are shown in Tables 2–4. The experimental values at EOL are in bold; those measured obtained during laboratory isochronal (30 min) annealing at 50 K steps are in italics.

## Appendix B. Phonon scattering parameters for soluble fission products

The FP concentrations were calculated with the ORIGEN 2 code [19]. The dynamically dissolved fraction of fission gases Xe, Cs, Kr was noted $g$ and taken as zero for the analysis of the results obtained after complete annealing. The dissolved fraction of Rb, Ba and Sr was noted $c$ and was kept as parameter for further discussion. The ionic radii used are those given by Shannon [25] and Zachariasen [26]. The results for 1 ton of fresh $UO_2$ and a burn-up of 34 GWd t$^{-1}$ are shown on Table 5. The inventory of the metallic FP obtained at bu = 34 GWd t$^{-1}$ and for 1 ton of fresh $UO_2$ is presented in Table 6.

Table 2
Experimental and calculated thermal conductivity values for bu ≈ 34 GWd t$^{-1}$, $T$ in K

| $T$ | Exp. $T_{irr} = 730$ bu = 34 before annealing | Exp. $T_{irr} = 730$ bu = 34 annealed at 1450 | Model $T_{irr} = 730$ bu = 34 before annealing | Model $T_{irr} = 730$ bu = 34 annealed at 1450 | Exp. $T_{irr} = 860$ bu = 34 before annealing | Exp. $T_{irr} = 860$ bu = 34 annealed at 1450 | Model $T_{irr} = 860$ bu = 34 before annealing | Model $T_{irr} = 860$ bu = 34 annealed at 1450 | Exp. $T_{irr} = 1020$ bu = 33 before annealing | Exp. $T_{irr} = 1020$ bu = 33 annealed at 1450 | Model $T_{irr} = 1020$ bu = 33 before annealing | Model $T_{irr} = 1020$ bu = 33 annealed at 1450 | Exp. $T_{irr} = 1210$ bu = 34 before annealing | Exp. $T_{irr} = 1210$ bu = 34 annealed at 1450 | Model $T_{irr} = 1210$ bu = 34 before annealing | Model $T_{irr} = 1210$ bu = 34 annealed at 1450 |
|---|---|---|---|---|---|---|---|---|---|---|---|---|---|---|---|---|
| 500 | **2.93** | **3.80** | 2.91 | 3.90 | **3.13** | **4.03** | 2.92 | 3.90 | **3.09** | **3.86** | 3.04 | 3.90 | **3.12** | **3.28** | 3.16 | 3.90 |
| 550 | **2.85** | **3.62** | 2.83 | 3.69 | **3.00** | **3.78** | 2.83 | 3.69 | **2.97** | **3.65** | 2.93 | 3.69 | **2.97** | **3.14** | 3.04 | 3.69 |
| 600 | **2.77** | **3.45** | 2.75 | 3.50 | **2.88** | **3.57** | 2.75 | 3.50 | **2.85** | **3.46** | 2.82 | 3.50 | **2.84** | **3.01** | 2.92 | 3.51 |
| 650 | **2.69** | **3.30** | 2.67 | 3.33 | **2.78** | **3.38** | 2.67 | 3.33 | **2.75** | **3.29** | 2.73 | 3.33 | **2.73** | **2.89** | 2.81 | 3.34 |
| 700 | **2.62** | **3.16** | 2.60 | 3.18 | **2.68** | **3.21** | 2.60 | 3.18 | **2.65** | **3.14** | 2.63 | 3.18 | **2.62** | **2.79** | 2.72 | 3.18 |
| 750 | **2.55** | **3.04** | 2.53 | 3.04 | **2.58** | **3.05** | 2.53 | 3.04 | **2.56** | **3.00** | 2.55 | 3.04 | **2.51** | **2.68** | 2.62 | 3.04 |
| 800 | ***2.47*** | **2.92** | 2.46 | 2.91 | **2.50** | **2.91** | 2.46 | 2.91 | **2.47** | **2.87** | 2.47 | 2.91 | **2.42** | **2.59** | 2.54 | 2.92 |
| 850 | ***2.40*** | **2.81** | 2.40 | 2.79 | **2.41** | **2.78** | 2.40 | 2.79 | **2.39** | **2.76** | 2.39 | 2.79 | **2.33** | **2.50** | 2.46 | 2.80 |
| 900 | ***2.34*** | **2.71** | 2.34 | 2.69 | **2.34** | **2.66** | 2.34 | 2.69 | **2.32** | **2.65** | 2.32 | 2.69 | **2.25** | **2.42** | 2.38 | 2.69 |
| 950 | ***2.29*** | **2.62** | 2.28 | 2.59 | **2.27** | **2.56** | 2.28 | 2.59 | **2.24** | **2.55** | 2.26 | 2.59 | **2.18** | **2.34** | 2.32 | 2.59 |
| 1000 | ***2.24*** | **2.53** | 2.21 | 2.49 | ***2.25*** | **2.46** | 2.21 | 2.49 | **2.18** | **2.45** | 2.21 | 2.49 | **2.11** | **2.27** | 2.26 | 2.50 |
| 1050 | ***2.20*** | **2.45** | 2.16 | 2.41 | ***2.16*** | **2.37** | 2.16 | 2.41 | **2.12** | **2.37** | 2.16 | 2.41 | **2.04** | **2.20** | 2.20 | 2.41 |
| 1100 | ***2.15*** | **2.37** | 2.11 | 2.33 | ***2.04*** | **2.28** | 2.11 | 2.33 | ***2.06*** | **2.29** | 2.11 | 2.33 | **1.98** | **2.14** | 2.16 | 2.33 |
| 1150 | ***2.10*** | **2.30** | 2.07 | 2.25 | ***1.98*** | **2.20** | 2.07 | 2.25 | ***2.00*** | **2.21** | 2.08 | 2.25 | **1.92** | **2.08** | 2.11 | 2.25 |
| 1200 | ***2.05*** | **2.23** | 2.05 | 2.18 | ***1.91*** | **2.13** | 2.05 | 2.18 | ***1.95*** | **2.14** | 2.05 | 2.18 | **1.86** | **2.02** | 2.08 | 2.19 |
| 1250 | ***1.97*** | **2.17** | 2.03 | 2.12 | ***1.90*** | **2.06** | 2.03 | 2.12 | ***1.88*** | **2.08** | 2.03 | 2.12 | ***1.81*** | **1.97** | 2.05 | 2.12 |
| 1300 | ***1.92*** | **2.11** | 2.01 | 2.06 | ***1.87*** | **1.99** | 2.01 | 2.06 | ***1.85*** | **2.02** | 2.01 | 2.06 | ***1.76*** | **1.92** | 2.02 | 2.06 |
| 1350 | ***1.90*** | **2.05** | 1.98 | 2.01 | ***1.85*** | **1.93** | 1.98 | 2.01 | ***1.82*** | **1.96** | 1.98 | 2.01 | ***1.72*** | **1.87** | 1.99 | 2.01 |
| 1400 | ***1.90*** | **1.99** | 1.95 | 1.96 | ***1.80*** | **1.87** | 1.95 | 1.96 | ***1.78*** | **1.90** | 1.95 | 1.96 | ***1.67*** | **1.82** | 1.95 | 1.96 |
| 1450 | ***1.90*** | **1.94** | 1.91 | 1.91 | ***1.80*** | **1.82** | 1.91 | 1.91 | ***1.74*** | **1.85** | 1.91 | 1.91 | ***1.63*** | **1.78** | 1.92 | 1.92 |

Table 3
Experimental and calculated thermal conductivity values for bu ≈ 52 GWd t$^{-1}$, $T$ in K

| $T$ | Exp. $T_{irr} = 680$ bu = 55 before annealing | Model $T_{irr} = 680$ bu = 55 before annealing | Model $T_{irr} = 680$ bu = 55 annealed at 1450 | Exp. $T_{irr} = 890$ bu = 51 before annealing | Exp. $T_{irr} = 890$ bu = 51 annealed at 1450 | Model $T_{irr} = 890$ bu = 51 before annealing | Model $T_{irr} = 890$ bu = 51 annealed at 1450 | Exp. $T_{irr} = 1100$ bu = 51 before annealing | Exp. $T_{irr} = 1100$ bu = 51 annealed at 1450 | Model $T_{irr} = 1100$ bu = 51 before annealing | Model $T_{irr} = 1100$ bu = 51 annealed at 1450 | Exp. $T_{irr} = 1300$ bu = 51 before annealing | Exp. $T_{irr} = 1300$ bu = 51 annealed at 1450 | Model $T_{irr} = 1300$ bu = 51 before annealing | Model $T_{irr} = 1300$ bu = 51 annealed at 1450 |
|---|---|---|---|---|---|---|---|---|---|---|---|---|---|---|---|
| 500 | **2.41** | 2.34 | 3.36 | **2.68** | **3.48** | 2.42 | 3.43 | **2.44** | **3.64** | 2.57 | 3.43 | **3.46** | **3.65** | 2.95 | 3.47 |
| 550 | **2.36** | 2.29 | 3.20 | **2.60** | **3.31** | 2.37 | 3.26 | **2.37** | **3.44** | 2.49 | 3.27 | **3.30** | **3.47** | 2.83 | 3.30 |
| 600 | **2.32** | 2.25 | 3.06 | **2.52** | **3.16** | 2.32 | 3.11 | **2.32** | **3.27** | 2.41 | 3.12 | **3.15** | **3.31** | 2.73 | 3.14 |
| 650 | **2.27** | 2.21 | 2.92 | **2.45** | **3.03** | 2.27 | 2.98 | **2.26** | **3.11** | 2.34 | 2.98 | **3.01** | **3.16** | 2.63 | 3.00 |
| 700 | **2.23** | 2.17 | 2.80 | **2.38** | **2.90** | 2.23 | 2.85 | **2.21** | **2.96** | 2.28 | 2.85 | **2.88** | **3.03** | 2.54 | 2.88 |
| 750 | **2.19** | 2.13 | 2.69 | **2.31** | **2.79** | 2.18 | 2.74 | **2.16** | **2.83** | 2.21 | 2.74 | **2.77** | **2.91** | 2.45 | 2.76 |
| 800 | **2.15** | 2.09 | 2.59 | **2.25** | **2.68** | 2.14 | 2.63 | **2.11** | **2.71** | 2.16 | 2.63 | **2.66** | **2.79** | 2.38 | 2.65 |
| 850 | | 2.06 | 2.49 | **2.19** | **2.58** | 2.10 | 2.53 | **2.06** | **2.59** | 2.10 | 2.53 | **2.56** | **2.69** | 2.30 | 2.55 |
| 900 | | 2.02 | 2.40 | **2.13** | **2.49** | 2.06 | 2.44 | **2.02** | **2.49** | 2.05 | 2.44 | **2.47** | **2.59** | 2.23 | 2.46 |
| 950 | | 1.97 | 2.32 | **2.08** | **2.40** | 2.01 | 2.35 | **1.98** | **2.40** | 2.00 | 2.35 | **2.38** | **2.50** | 2.17 | 2.37 |
| 1000 | | 1.92 | 2.24 | **2.02** | **2.32** | 1.96 | 2.28 | **1.94** | **2.31** | 1.96 | 2.28 | **2.30** | **2.42** | 2.12 | 2.29 |
| 1050 | | 1.88 | 2.17 | **1.96** | **2.25** | 1.92 | 2.20 | **1.90** | **2.23** | 1.93 | 2.20 | **2.23** | **2.34** | 2.07 | 2.22 |
| 1100 | | 1.85 | 2.10 | **1.91** | **2.18** | 1.88 | 2.13 | **1.86** | **2.15** | 1.90 | 2.13 | **2.16** | **2.26** | 2.02 | 2.15 |
| 1150 | | 1.83 | 2.04 | **1.87** | **2.11** | 1.86 | 2.07 | **1.83** | **2.08** | 1.87 | 2.07 | **2.09** | **2.19** | 1.98 | 2.08 |
| 1200 | | 1.82 | 1.98 | **1.82** | **2.05** | 1.85 | 2.01 | **1.80** | **2.01** | 1.86 | 2.01 | **2.03** | **2.13** | 1.95 | 2.02 |
| 1250 | | 1.82 | 1.93 | **1.78** | **1.99** | 1.85 | 1.95 | **1.79** | **1.95** | 1.85 | 1.95 | **1.97** | **2.07** | 1.91 | 1.97 |
| 1300 | | 1.82 | 1.88 | **1.75** | **1.94** | 1.84 | 1.90 | **1.79** | **1.89** | 1.85 | 1.90 | **1.92** | **2.01** | 1.89 | 1.92 |
| 1350 | | 1.80 | 1.83 | **1.72** | **1.89** | 1.83 | 1.86 | **1.78** | **1.84** | 1.83 | 1.86 | **1.87** | **1.95** | 1.85 | 1.87 |
| 1400 | | 1.78 | 1.79 | **1.69** | **1.84** | 1.80 | 1.82 | **1.77** | **1.79** | 1.80 | 1.82 | **1.82** | **1.90** | 1.82 | 1.83 |
| 1450 | | 1.76 | 1.76 | **1.68** | **1.79** | 1.78 | 1.78 | **1.77** | **1.78** | 1.78 | 1.78 | **1.77** | **1.85** | 1.79 | 1.79 |

Table 4
Experimental and calculated thermal conductivity values for bu ≈ 82 GWd t$^{-1}$ and bu ≈ 94 GWd t$^{-1}$

| $T$ | Exp. $T_{irr}$ = 700 K bu = 82 before annealing | Model $T_{irr}$ = 700 K bu = 82 before annealing | Model $T_{irr}$ = 700 K bu = 82 annealed at 1450 K | Exp. $T_{irr}$ = 730 K bu = 96 before annealing | Model $T_{irr}$ = 730 K bu = 96 before annealing | Model $T_{irr}$ = 730 K bu = 96 annealed at 1450 K | Exp. $T_{irr}$ = 1490 K bu = 92 before annealing | Exp. $T_{irr}$ = 1490 K bu = 92 annealed at 1450 K | Model $T_{irr}$ = 1490 K bu = 92 before annealing | Model $T_{irr}$ = 1490 K bu = 92 annealed at 1450 K |
|---|---|---|---|---|---|---|---|---|---|---|
| 500 | **2.18** | 2.20 | 2.88 | **2.06** | 1.99 | 2.67 | **2.50** | **2.63** | 2.59 | 2.74 |
| 550 | **2.16** | 2.18 | 2.76 | **2.04** | 1.98 | 2.57 | **2.42** | **2.55** | 2.49 | 2.62 |
| 600 | **2.14** | 2.16 | 2.65 | **2.03** | 1.97 | 2.47 | **2.34** | **2.47** | 2.39 | 2.52 |
| 650 | **2.12** | 2.14 | 2.54 | **2.01** | 1.96 | 2.38 | **2.27** | **2.40** | 2.31 | 2.42 |
| 700 | **2.10** | 2.12 | 2.45 | **1.99** | 1.94 | 2.29 | **2.20** | **2.33** | 2.23 | 2.34 |
| 750 | **2.08** | 2.10 | 2.36 | **1.97** | 1.93 | 2.21 | **2.14** | **2.26** | 2.15 | 2.25 |
| 800 | **2.07** | 2.08 | 2.27 | **1.95** | 1.92 | 2.14 | **2.08** | **2.20** | 2.08 | 2.18 |
| 850 | | 2.06 | 2.20 | | 1.91 | 2.07 | **2.02** | **2.14** | 2.02 | 2.10 |
| 900 | | 2.03 | 2.13 | | 1.89 | 2.00 | **1.97** | **2.08** | 1.95 | 2.04 |
| 950 | | 1.96 | 2.06 | | 1.83 | 1.94 | **1.92** | **2.03** | 1.90 | 1.97 |
| 1000 | | 1.88 | 2.00 | | 1.77 | 1.88 | **1.87** | **1.98** | 1.85 | 1.92 |
| 1050 | | 1.84 | 1.94 | | 1.73 | 1.83 | **1.82** | **1.93** | 1.81 | 1.86 |
| 1100 | | 1.81 | 1.88 | | 1.70 | 1.78 | **1.78** | **1.89** | 1.76 | 1.81 |
| 1150 | | 1.78 | 1.83 | | 1.68 | 1.73 | **1.74** | **1.84** | 1.72 | 1.76 |
| 1200 | | 1.76 | 1.78 | | 1.66 | 1.69 | **1.70** | **1.80** | 1.69 | 1.72 |
| 1250 | | 1.73 | 1.74 | | 1.63 | 1.65 | **1.66** | **1.76** | 1.65 | 1.67 |
| 1300 | | 1.69 | 1.70 | | 1.61 | 1.61 | **1.62** | **1.72** | 1.62 | 1.63 |
| 1350 | | 1.66 | 1.66 | | 1.57 | 1.58 | **1.59** | **1.69** | 1.59 | 1.60 |
| 1400 | | 1.62 | 1.62 | | 1.54 | 1.55 | **1.56** | **1.65** | 1.56 | 1.57 |
| 1450 | | 1.59 | 1.59 | | 1.52 | 1.52 | **1.52** | **1.62** | 1.54 | 1.54 |

## Appendix C. Prediction of the physical state of volatile fission products with a gas diffusion/precipitation/release model

The model process can be sketched as follows: the fission gas, thermodynamically insoluble in the matrix, is initially injected in the lattice where atomic mobility induces precipitation into bubbles. Since collisions with fission fragment recoil cascades tend to re-inject gas into the lattice, if atomic diffusion is slow, a large fraction of gas may be kept in dynamical solution. This sustains the diffusion flow to grain boundaries and open porosity from which radiation re-solution is less effective. In $UO_2$, this occurs at irradiation temperatures below 1000–1200 K. In contrast, at higher temperatures, most of the gas precipitates into bubbles and pores, through which it can finally escape from the pellet.

A convenient method for describing these simultaneous mechanisms is the reaction-rate equation formalism by which approximate analytical solutions of the differential equation system can be found (see, e.g., [27]). The model calculates the partition of the gas in the different states starting from a number of kinetic (gas creation rate, diffusion coefficient and re-solution rate) and structural (measured grain size, radii and concentrations of the various bubble populations) parameters. In our context, a relevant value of GIS can only be obtained by considering the entire irradiation history of the sample and, when laboratory annealing is involved, the applied temperature programme. The simplest rate equations linking the amounts of fission gas present in dynamical solution, $c(t) = \text{GIS}\ \beta t$, and in intra-granular bubbles, $b(t)$, are

$$\begin{cases} \dfrac{\mathrm{d}c(t)}{\mathrm{d}t} = Wc(t) + \eta b(t) + \beta, \\ \dfrac{\mathrm{d}b(t)}{\mathrm{d}t} = Kc(t) - \eta b(t), \end{cases} \tag{C.1}$$

where $K = k_{sc}^2 D$, $W = -(H + K)$, $H = k_{gb}^2 D$, $\beta$ is the gas creation rate, $\eta$ is the experimentally measured fission fragment re-solution time constant [28], and $D$ the diffusion coefficient. In this formalism $k_{sc}^2$ and $k_{gb}^2$ represent the various sink strengths, whereby in our case two main sinks are labelled with the index sc (precipitation through the specific surface of intra-granular bubbles), and gb (capture of gas in grain boundaries). The individual sink strengths can be calculated if a complete description of the bubble and pore size distribution in the sample is available. This distribution was measured in several samples irradiated under different conditions by manual image analysis using scanned TEM images (0.01-μm scale), SEM images (0.1-μm scale) and optical ceramographs for the porosity. The distribution functions obtained for different burn-ups were fitted by

Table 5
Inventory and contribution to the phonon scattering parameter of actinides and soluble FP at bu = 34 GWd t$^{-1}$ and for 1 metric tonne of fresh $UO_2$

| Element | Atomic weight $M_i$ (g mol$^{-1}$) | Ionic radius $r_i$ (nm) | Inventory (mol) | Solubility limit in solid $UO_2$ | Atomic fraction in the solution ($y_i$) if $g = 0$ and $c = 0.24$ | Mass-difference contribution to $\Gamma_2$ $y_i\left(\frac{\bar{M}-M_i}{\bar{M}}\right)^2$ if $g = 0$ and $c = 0.24$ | Radius-difference contribution to $\Gamma$ $y_i\varepsilon\left(\frac{\bar{r}-r_i}{\bar{r}}\right)^2$ if $g = 0$ and $c = 0.24$ |
|---|---|---|---|---|---|---|---|
| U | 237.32 | 0.089 | $4.04\times10^{3}$ | 1 | 0.965670 | 0.0002520 | 0.0002386 |
| Xe | 134.01 | 0.048 | 35.5 | $g = 0$ | 0 | 0 | 0 |
| Cs | 134.87 | 0.188 | 24.7 | $g = 0$ | 0 | 0 | 0 |
| Kr | 84.98 | 0.054 | 5.66 | $g = 0$ | 0 | 0 | 0 |
| Nd | 144.75 | 0.098 | 3.09 | 1 | 0.007216 | 0.0010432 | 0.0076199 |
| Zr | 93.17 | 0.084 | 47.3 | 1 | 0.011058 | 0.0039951 | 0.0036770 |
| Ce | 140.99 | 0.087 | 18.3 | 1 | 0.004284 | 0.0006728 | 0.0002469 |
| Pu | 239.14 | 0.086 | 7.32 | 1 | 0.001712 | 0.0000010 | 0.0002125 |
| Ba | 137.80 | 0.135 | 11.5 | $c = 0.24$ | 0.000644 | 0.0001083 | 0.0170527 |
| La | 139.00 | 0.103 | 9.70 | 1 | 0.002268 | 0.0003717 | 0.0056418 |
| Pr | 141.00 | 0.099 | 8.84 | 1 | 0.002068 | 0.0003247 | 0.0025303 |
| Sr | 89.19 | 0.118 | 13.0 | $c = 0.24$ | 0.000732 | 0.0002796 | 0.0076710 |
| Sm | 149.02 | 0.096 | 5.43 | 1 | 0.001270 | 0.0001664 | 0.0007090 |
| Y | 89.00 | 0.090 | 7.15 | 1 | 0.001673 | 0.0006408 | 0.0000156 |
| Rb | 86.41 | 0.152 | 5.48 | $c = 0.24$ | 0.000307 | 0.0001220 | 0.0152825 |
| Te | 129.49 | 0.097 | 2.96 | 1 | 0.000693 | 0.0001376 | 0.0005389 |
| Np | 236.99 | 0.087 | $5.00\times10^{-1}$ | 1 | 0.000117 | 0.0000000 | 0.0000067 |
| Pm | 147.04 | 0.097 | $7.58\times10^{-1}$ | 1 | 0.000177 | 0.0000243 | 0.0001379 |
| Eu | 153.06 | 0.107 | $3.54\times10^{-1}$ | 1 | 0.000083 | 0.0000098 | 0.0003177 |
| Gd | 156.08 | 0.105 | $9.62\times10^{-2}$ | 1 | 0.000023 | 0.0000025 | 0.0000740 |
| Am | 241.04 | 0.098 | $1.82\times10^{-2}$ | 1 | 0.000004 | 0.0000000 | 0.0000037 |
| Th | 230.62 | 0.108 | $1.91\times10^{-5}$ | 1 | 0.000000 | 0.0000000 | 0.0000000 |
| Nb | 93.08 | 0.064 | $2.49\times10^{-5}$ | 1 | 0.000000 | 0.0000000 | 0.0000000 |
| Pa | 231.03 | 0.118 | $5.83\times10^{-6}$ | 1 | 0.000000 | 0.0000000 | 0.0000000 |
| Cm | 243.68 | 0.097 | $1.70\times10^{-6}$ | 1 | 0.000000 | 0.0000000 | 0.0000000 |

Table 6
Inventory of the considered metallic FP at bu = 34 GWd t$^{-1}$ and for 1 metric tonne of fresh $UO_2$

| Element | Inventory (mol) | Weight (g) | Volume fraction (%) in the composite material |
|---|---|---|---|
| Mo | $3.68\times10^{1}$ | $3.58\times10^{3}$ | 0.35433 |
| Ru | $1.72\times10^{1}$ | $1.75\times10^{3}$ | 0.17326 |
| Tc | 8.92 | $8.83\times10^{2}$ | 0.08735 |
| Rh | 4.54 | $4.68\times10^{2}$ | 0.04625 |
| Pd | 3.17 | $3.35\times10^{2}$ | 0.03312 |
| Te | 2.96 | $3.84\times10^{2}$ | 0.03796 |
| Sn | $3.25\times10^{-1}$ | $3.97\times10^{1}$ | 0.00393 |
| Cd | $1.79\times10^{-1}$ | $2.02\times10^{1}$ | 0.00200 |
| Sb | $8.82\times10^{-2}$ | $1.08\times10^{1}$ | 0.00107 |
| Ag | $8.73\times10^{-2}$ | 9.52 | 0.00094 |
| In | $2.17\times10^{-2}$ | 2.50 | 0.00025 |

log-normal laws. The bubble concentrations are plotted in Fig. 4, where the following features can be remarked:

- At constant irradiation temperature, the concentration of small intra-granular bubbles, which define the value of $k_{sc}^2$, attains a steady state at burn-ups of the order of 20 GWd t$^{-1}$, and does not effectively change at higher burn-ups.

  The bubbles-radius distribution (Fig. 4) was interpolated by a log-normal distribution and the obtained function $\Lambda(r)$ is defined by

$$\Lambda(r) = \frac{1}{(r-r_0)\sigma\sqrt{2\pi}}\exp\left\{-\frac{1}{2\sigma^2}(\log(r-r_0)-\mu)\right\}$$

  with $r_0 = 5\times10^{-10}$ m, $\mu = -24.73$, $\sigma = 1.697$, and the bubbles concentration is defined by $4.12\times10^{8}$ $\Lambda(r)$ (cm$^{-3}$).
- The effect of burn-up is limited to a class of bubbles and pores in the size range from approximately 0.1 μm to 1 μm, whose fractional volume markedly increases with burn-up, but whose concentration remains low and does *not* significantly affect the value of $k_{sc}^2$. The pore-size concentrations obtained at dif-

ferent burn-ups were fitted by different log-normal laws (Fig. 4).

- The occurrence of rim restructuring produces a decrease in intra-granular bubble concentration, but a strong increase in $k_{gb}^2$ (pseudo-polygonisation), so that the value of GIS is affected negatively.

The general formulation of the rate equation for variable sink strength coefficients is rather complex [28,29]. However, simplified expressions can be applied in our case [27]:

$$k_{sc}^2 = \sum_i 4\pi r_i N_i; \quad \mathsf{H} = \frac{3L(t)G}{(1-3G)};$$
$$\mathsf{L}(t) = k_{sc}^2 - \eta\left\langle \frac{b(t)}{c(t)} \right\rangle;$$
$$\mathsf{G} = -\frac{1}{L(t)\alpha_g^2} + \frac{\coth(\alpha_g\sqrt{L(t)/D})}{\alpha_g\sqrt{L(t)/D}}, \tag{C.2}$$

where

$$\left\langle \frac{b(t)}{c(t)} \right\rangle = \int_0^t \frac{b(t')}{c(t')}\frac{\mathrm{d}t'}{t}$$

is the arithmetic time average, $r_i$ are the bubble radii and $N_i$ the respective volume concentrations; $\alpha$ is the grain radius.

The solution of the differential system between times $t_0$ and $t$ is

$$\begin{pmatrix} c(t) \\ b(t) \end{pmatrix} = C_1 \mathrm{e}^{x_1 t}\begin{pmatrix} x_1+\eta \\ K \end{pmatrix} + C_2 \mathrm{e}^{x_2 t}\begin{pmatrix} x_2+\eta \\ K \end{pmatrix} - \begin{pmatrix} c_a \\ b_a \end{pmatrix}, \tag{C.3}$$

where $x_1$ and $x_2$ are the roots of the equation: $x^2 - (W-\eta)x - (W\eta+\eta K) = 0$ and the constants $C_1$ and $C_2$ are

$$C_1 = \frac{C_0 K - b_0(x_2+\eta)}{K(x_1-x_2)}, \quad C_2 = \frac{b_0(x_1+\eta) - KC_0}{K(x_1-x_2)}$$

with

$$C_0 = c_a + c(t_0), \quad b_0 = b_a + b(t_0)$$

where

$$c_a = -\beta/(W+K) \quad \text{and} \quad b_a = -\beta K/(W\eta+\eta K).$$

The assumed periodic diffusion domain is one grain of constant diameter equal to the diameter of the initially sintered structure, except for samples presenting a rim structure at EOL, where subgrains of 0.3 μm size are progressively formed during this restructuring fully occurring at burn-ups higher than 70 GWd t$^{-1}$ and irradiation temperatures lower than about 950 K. The equation coefficients were adapted to take into account this grain polygonisation process. The grain size, including the effect of the rim formation is expressed as

$$\alpha_g(m) = \frac{9.7\times10^{-6}}{1+30\left[1+\exp\left(\frac{T_{irr}-950}{30}\right)\right]^{-1}\left[1+\exp\left(\frac{70-bu}{2}\right)\right]^{-1}}.$$

The diffusion coefficient $D$ for fission gas in irradiated $UO_2$ consists of three components: a high temperature intrinsic diffusion coefficient, $D_1$, an intermediate component, $D_2$, enhanced by radiation, and an almost a-thermal component, $D_3$, predominant at low temperatures, and proportional to the fission rate.

The value of $D_1$, evaluated by Hiernaut from Knudsen effusion/release experiments [6] is expressed as

$$D_1(\mathrm{m^2\,s^{-1}}) = 15\times10^{-8}\exp\left(-\frac{\Delta H}{kT}\right),$$

where $\Delta H$ is a burn-up-dependent diffusion enthalpy approximated by

$$\Delta H = ((1.10\times10^{-3}T - 3.07)\mathrm{bu} + 493.11)10^3 \quad (\mathrm{J/mol}), \tag{C.4}$$

where bu is in GWd t$^{-1}$, and $T$ in K. The formula was experimentally validated between 20 and 100 GWd t$^{-1}$ and 800 K $< T <$ 2500 K [6].

The two other radiation-enhanced contributions to the diffusion coefficient are [30]:

$$D_2(\mathrm{m^2\,s^{-1}}) = 1.38\times10^{-16}R_f^{1/2}\exp(-13\,800/T)$$

and

$$D_3(\mathrm{m^2 s^{-1}}) = 7.67\times10^{-22}R_f\exp(-2785/T), \tag{C.5}$$

where $R_f = 1.18$ bu is the fuel fission rate (W/g$_U$).

The gas concentration was calculated by an iterative method using the analytical solution at each time step, and evaluating the change of the different parameters, in particular the grain size, between two time steps (Fig. 5).

For an isothermal irradiation in the absence of rim formation it can be seen that the *fraction* of gas-in-solid, GIS, is approximately independent of burn-up. This means that the *absolute* quantity of gas in dynamical solution increases linearly with burn-up. At temperatures where the diffusion coefficient $D$ is high, GIS is very low and has no effect on the thermal conductivity. The same occurs in samples displaying the rim structure, where GIS is very low.

## References

[1] M. Kinoshita, T. Sonoda, S. Kitajima, A. Sasahara, E. Kolstad, H. Matzke, V.V. Rondinella, A.D. Stalios, C.T. Walker, I.L.F. Ray, M. Sheindlin, D. Halton, C. Ronchi, in: Proceedings of ANS Topical Meeting on LWR Fuel Performance, Park City, Utah, USA, 9–13 April 2000, ISBN-0-89448-656-X.

[2] M. Sheindlin, D. Halton, M. Musella, C. Ronchi, Rev. Sci. Instrum. 69 (1998) 1426.
[3] J.K. Fink, J. Nucl. Mater. 279 (2000) 1.
[4] C. Ronchi, M. Sheindlin, M. Musella, J. Appl. Phys. 85 (1999) 776.
[5] P.G. Klemens, Phys. Rev. 119 (1960) 507.
[6] J.P. Hiernaut, European Institute for Transuranium Elements, Karlsruhe (Germany), in press.
[7] W. Wiesenack, in: Proceedings of ANS International Topical Meeting on LWR Fuel Performance, Portland, Oregon, USA, 2–6 March 1997, ISBN-0-89448-616-0.
[8] S. Ishimoto, M. Hirai, K. Ito, Y. Korei, J. Nucl. Sci. Technol. 31 (1994) 796.
[9] Y. Ambegaoker, Trans. Am. Nucl. Soc. 9 (1966) 488.
[10] C. Duriez, J.P. Alessandri, T. Gervais, Y. Philipponneau, J. Nucl. Mater. 277 (2000) 143.
[11] S. Fukushima, T. Ohmichi, A. Maeda, M. Hanada, J. Nucl. Mater. 116 (1983) 287.
[12] S. Fukushima, T. Ohmichi, A. Maeda, H. Watanabe, J. Nucl. Mater. 102 (1981) 30.
[13] D.P. Preston, C. Barrett, P. Fassina, K. Mills, N. Zaghini, High Temp.-High Press. 21 (1989) 287.
[14] B. Abeles, Phys. Rev. 131 (1963) 507.
[15] S. Fukushima, T. Ohmichi, A. Maeda, M. Hanada, J. Nucl. Mater. 114 (1983) 260.
[16] S. Fukushima, T. Ohmichi, A. Maeda, H. Watanabe, J. Nucl. Mater. 105 (1982) 201.
[17] P.S. Murti, C.K. Mathews, High Temp.-High Press. 22 (1990) 379.
[18] G. Leibfried, E. Schlömann, Nachr. Akad. Wiss. Göttingen. Math. Phys. KI 2-A (1954) 71.
[19] A.G. Croff, Nucl. Technol. 62 (1983) 335.
[20] H. Kleykamp, J. Nucl. Mater. 131 (1985) 221.
[21] A. Eucken, Forsch. Gebiete Ingenieur. B 3 (1932) 6.
[22] M.V. Krishnaiah, G. Seenivasan, P.S. Murti, C.K. Mathews, J. Nucl. Mater. 306 (2002) 10.
[23] S. Yamanaka, K. Kurosaki, T. Matsuda, M. Uno, J. Nucl. Mater. 294 (2001) 99.
[24] J. Spino, D. Papaioannou, J. Nucl. Mater. 281 (2000) 146.
[25] R.D. Shannon, Acta Crystallogr. A 32 (1976) 751.
[26] W.H. Zachariasen, Acta Crystallogr. 23 (1967) 558.
[27] C. Syros, J. Sakellaridis, C. Ronchi, J. Nucl. Mater. 168 (1989) 65.
[28] C. Ronchi, P.T. Elton, J. Nucl. Mater. 140 (1986) 228.
[29] M. Gardani, C. Ronchi, Nucl. Sci. Technol. 107 (1991) 315.
[30] J.A. Turnbull, in: International Symposium on Fission Gas Behaviour in Water Reactor Fuels, 26–29 September 2000, Cadarache, France, ISBN-92-64-19715-X.